Volume 22 (2) 2023 Page 76 - 87

Mekanika: Majalah Ilmiah Mekanika

Predicting the Drag Coefficient Characteristics of Ocean Bottom Unit (OBU) Float Array Model for Early Warning Tsunami Systems Using Computational Fluid Dynamics (CFD) Method

Yudiawan Fajar Kusuma[1*], Ilham Hariz[2], Hanni Defianti[3], Buddin Al Hakim[1], Arfis Maydino F. Putra[4]

1 Research Center for Hydrodynamics Technology, National Research and Innovation Agency, BRIN, Surabaya, Indonesia
2 Directorate of Laboratory Management, Research Facilities, and Science and Technology Park, South Tangerang, Indonesia
3 Research Center for Aeronautics Technology, National Research and Innovation Agency, Bogor, Indonesia
4 Department of Naval Architecture and Ocean Engineering, Marine Hydro-Science and Engineering Laboratory, Osaka University, Osaka, Japan

*Corresponding Author's email address: yudi018@brin.go.id

Keywords:
Floater OBU
Computational fluid dynamics
Drag coefficient
INA-TEWS

Abstract
The early tsunami warning system encompasses several complex components, one of which is the Ocean Bottom Unit (OBU) floater. This paper discusses the performance of various types of floater arrays for tsunami early warning systems using Computational Fluid Dynamics (CFD) simulations. The study focuses on coefficients, especially the drag coefficient, and the influence of the number of float arrangements on the flow pattern around the buoy or Ocean Bottom Unit (OBU) array. Among the five numerical simulation models, the six-couple floater has the highest drag and lowest lift coefficients, while the single floater has the lowest drag coefficient. The percentage of difference in drag coefficient between single floater and couple series floater is quite significant, reaching up to 50%. The moment coefficient is also affected by the number of floaters, with a series of five couple floaters having the highest moment coefficient at a Reynolds number (*Re*) of 2×10^6. The results indicate that the flow pattern becomes more complex as the number of floater arrays increases, which leads to more vortices between the floater, resulting in increased turbulence and drag coefficient.

1 Introduction

Indonesia, as an archipelagic country located in the Ring of Fire, is vulnerable to natural disasters such as earthquakes, volcanic eruptions, tsunamis, and sea-level rise [1-3]. Indonesia is geologically situated at the convergence of four major active tectonic plates and several minor plates. The four major active plates are the Eurasian, Indo-Australian, Pacific, and Philippine Sea Plates [4,5]. The speed and direction of active movement between these plates vary [5-7], leading to earthquakes and tsunamis.

https://dx.doi.org/10.20961/mekanika.v22i2.75079

Revised 17 August 2023; received in revised version 27 August 2023; Accepted 18 September 2023
Available Online 30 Septmber 2023

2579-3144

In Indonesia, there are at least 13 megathrust zones [7,8], which have a high potential for significant earthquakes and tsunamis that can have a major impact on the lives and economy of the population. More than 245 recorded tsunami events occurred in Indonesia between 1600 and 2022. [2,9,10]. However, this number is likely underestimated as a proper recording of tsunami events was not consistently conducted between 1600 and 1800. Almost all coastal regions and cities in Indonesia are considered highly risky, with estimated tsunami heights exceeding three meters. In 2015, the population affected by tsunamis in Indonesia was 3.7×10^6 people, projected to reach 4.4×10^6 people by 2030 [11,12]. As an illustration of the economic losses resulting from the 2004 Aceh earthquake and tsunami, the total damages amounted to 48 trillion Indonesian Rupiah [13].

The Indonesian Tsunami Early Warning System (INA-TEWS) became operational in 2008 to reduce the risk and casualties from tsunamis. The system is designed to detect tsunamis [14,15]. However, the system requires support to function optimally. The 2018 tsunamis in Palu and the Sunda Strait, which resulted in significant loss of life, indicate that the early warning system needs to be improved to minimize casualties from tsunami events. A buoy-based tsunami detection system is one technology that can be utilized for early tsunami detection. An Ocean Bottom Unit (OBU) and a Surface Buoy are the components of the tsunami buoy system. Offshore buoys provide initial information on sea-level anomalies [15,16], enabling accurate early tsunami warnings. The OBU continuously communicates with the surface buoy through underwater acoustic modems. The surface buoy acts as a receiver for data from the OBU and transmits that data via satellite to the tsunami monitoring center at the Read Down Station (RDS) on land. In order to ensure the proper functioning of the OBU, its reliability at working depths needs to be assured.

Various improvements and modifications have been made to each INA-TEWS equipment to enhance the accuracy of tsunami disaster prediction. Figure 1 shows the developed OBU floater system used in INA-TEWS. The OBU floater system can be installed underwater and on the water surface in horizontal or vertical configurations. The OBU floater system is a marker for the OBU equipment and provides resistance to wind and water wave forces, preventing the OBU from drifting easily. Additionally, sensors are installed inside the float to receive and transmit data to satellites. In some cases, telecommunication antennas and meteorological sensors are mounted within the float. Therefore, a study is needed to design a model for the OBU float system that can withstand wind and water wave forces. The OBU floater system is typically spherical, with individual floats or in a circular formation. It is because a spherical shape provides balanced forces compared to other shapes. According to Sadraey et al. [17], the drag coefficient for a spherical model when the Reynolds number (*Re*) at $\leq 2 \times 10^5$ is 0.5, while for $Re \geq 2 \times 10^6$, it is 0.2. Similarly, Almedeij et al. [18] states that the drag coefficient for a spherical model when $Re \geq 2 \times 10^6$ is 0.2.

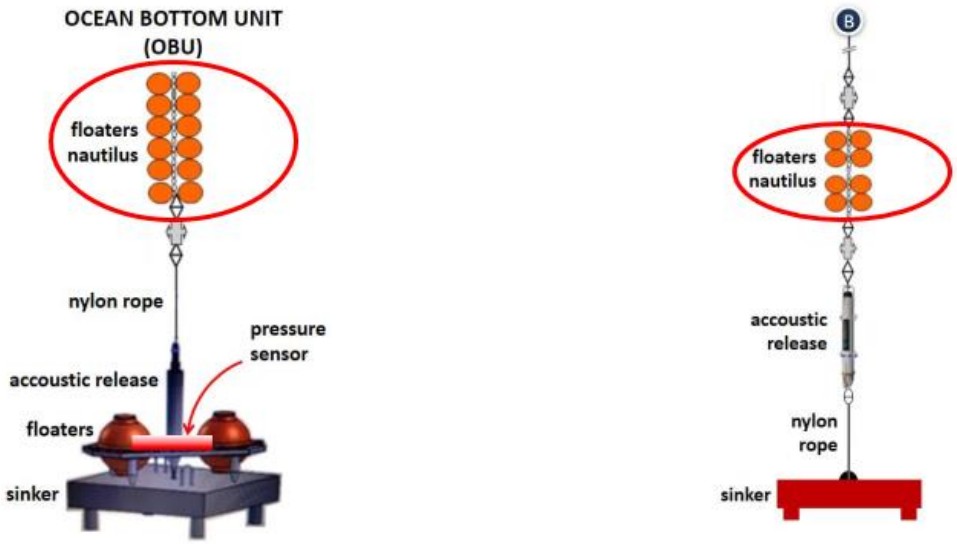

Figure 1. Various types of OBU floaters [1]

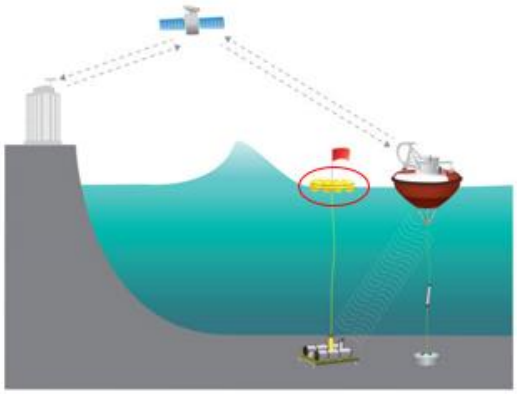

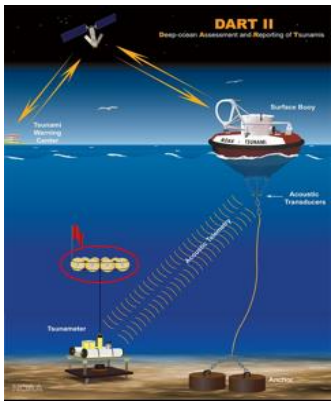

Figure 1. *Cont.*

Only now, few references discuss the models of OBU floater systems, as most of the research has focused on the OBU equipment itself or buoy. As done by Irfan et al. [19], a study was conducted on the placement of the mooring buoy and Ocean Bottom Unit (OBU) for the Indonesian Tsunami Early Warning System (INA-TEWS) on the seafloor. Nugroho et al. [11] investigated the design and structural analysis of the OBU's underwater device for the INA-TEWS using Finite Element Method (FEM) and testing. Arifin et al. [20] also studied the design of the Buoy Glider to support the tsunami early warning system using Computational Fluid Dynamics (CFD). Therefore, this study aims to focus on the coefficients involved in several models of the OBU floater system. One of the methods to be used in this research is Computational Fluid Dynamics (CFD). Compared to experimental methods, the CFD method has several advantages, such as optimizing the desired model design, more affordable cost, and the ability to visualize flow patterns. In this paper, two variations will be explored: Reynolds number variation and variations in the floater system models. Furthermore, numerical simulations will be conducted horizontally using air as the medium. The software used is commercial software, namely ANSYS version 2023 R1, which is licensed by the National Research and Innovation Agency. Space claim, fluent mesh, fluent, and CFD-post are the ANSYS modules used. The output of this numerical simulation includes the drag, lift, and moment coefficients, as well as flow visualization around the floater system models. The numerical simulation results are expected to be used as initial predictions to optimize the shape and float system of the buoy before conducting laboratory testing or creating prototypes.

2 Experimental Methods

The finite volume method is the Computational Fluid Dynamics (CFD) method. It is because the flow that occurs is external. CFD method consists of three stages: pre-processing, processing, and post-processing, as shown in Figure 2. The pre-processing stage is the initial and most crucial phase in CFD as it significantly influences the CFD results. It involves creating or checking the geometry, defining the computational domain, generating the mesh, selecting the solution equations, and determining the desired parameters.

Proper modeling and balance accuracy and available constraints are essential to obtain realistic simulation results. The processing stage marks the commencement of numerical calculations by the software once all the necessary settings have been finalized. This stage primarily involves monitoring the convergence of the numerical computations to ensure the accuracy and reliability of the results. Lastly, the post-processing stage is the final phase of the CFD analysis. It enables the extraction of desired outputs, such as coefficients, forces, pressure and velocity distributions, velocity streamlines, and other relevant information. This stage enables the visualization and interpretation of the simulation results in order to obtain insights into the phenomena under investigation.

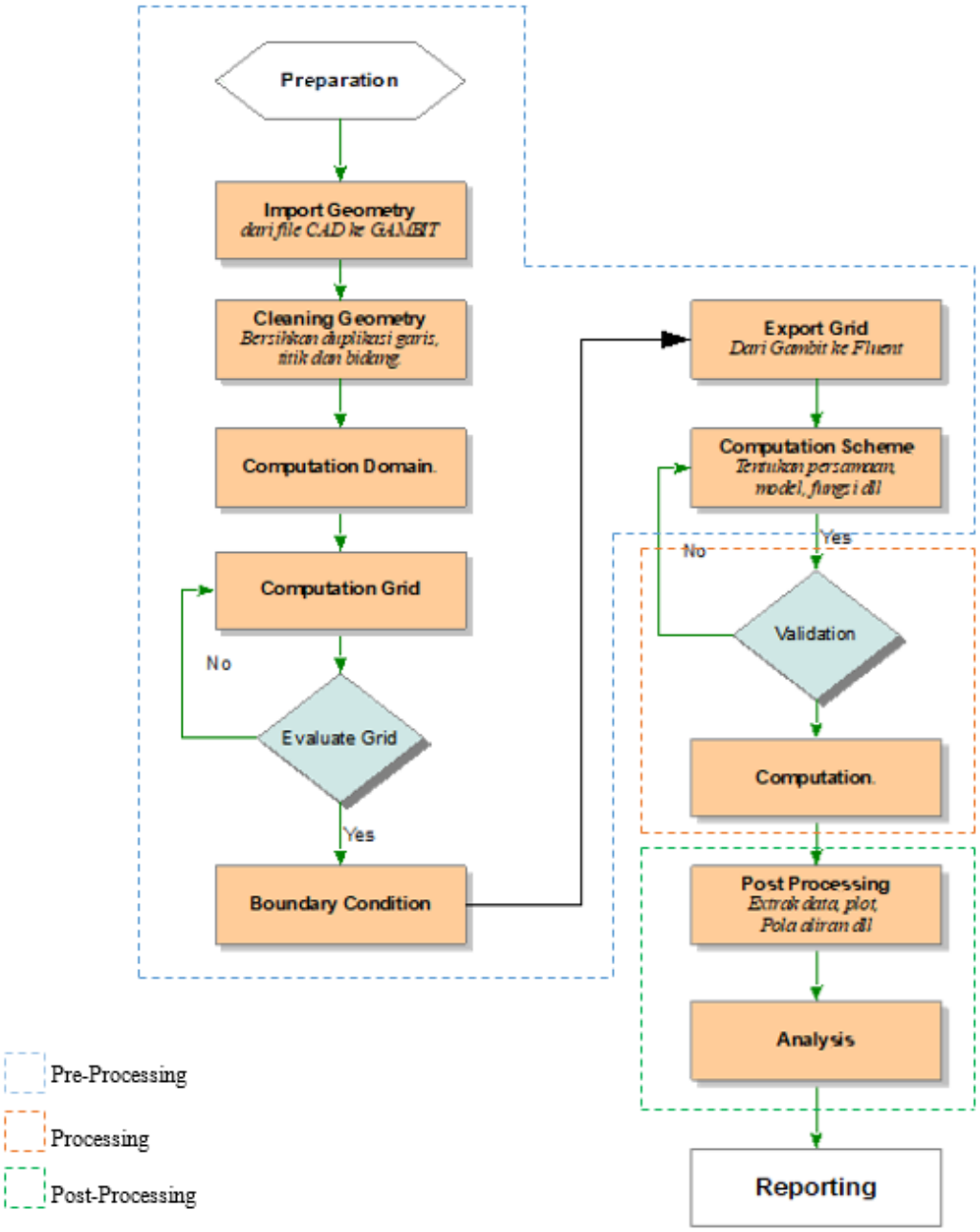

Figure 2. Flowchart of the CFD procedure [21]

2.1 Geometry

CATIA V5 software was used to build a geometry, which was then exported to the ANSYS SpaceClaim module within the software for geometry checking to ensure its suitability or identify any necessary improvements before proceeding further. The ANSYS SpaceClaim module is a 3D modeling application that may be used for geometry creation and refinement. There are several considerations to remember when creating geometry for CFD modeling, such as establishing initial coordinate points to facilitate parameter input and ensuring the use of appropriate unit systems, as they can influence the CFD results [22]. The table below contains the detailed dimensions of the OBU floater model. The distance between each float is equal to *D*/2. However, the model created in this study utilizes the bottom-up technique, where the geometry is constructed starting from the most fundamental unit, which is points. The points are then connected to form straight lines, which are further assembled to create surfaces, which are finally transformed into a volume [23]. As shown in Figure 3, the models to be simulated comprise a single OBU floater, a 4-unit couples OBU floater, a 5-unit couples OBU floater, and a 6-unit couples OBU floater.

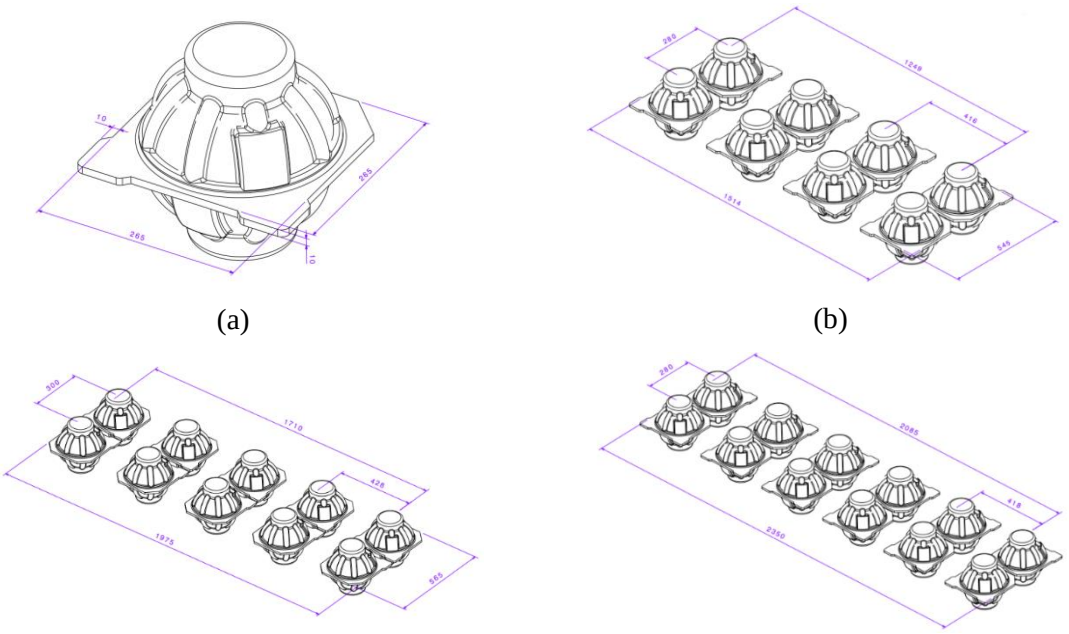

(a) (b)

(c) (d)

Figure 3. Floater OBU model: (a) Single, (b) 4 couples, (c) 5 Couples, and (d) 6 Couples

2.2 Domain and mesh

Following the construction of the geometry, the computational domain must be defined. The computational domain should not be affected by the presence of the models for free-flow cases. In this study, the computational domain in this study has a distance of 15 times the length of the model (B) in the forward, right, left, upward, and downward directions, while the back side has a distance of 31 times the length of the model (B). The computational area's size (Figure 4) is determined based on a study conducted by Bruno and Khris [24], where the area is not divided to avoid generating many mesh sizes. Additionally, the large size of the domain is optimized to prevent flow recirculation, which can impact the CFD results [25].

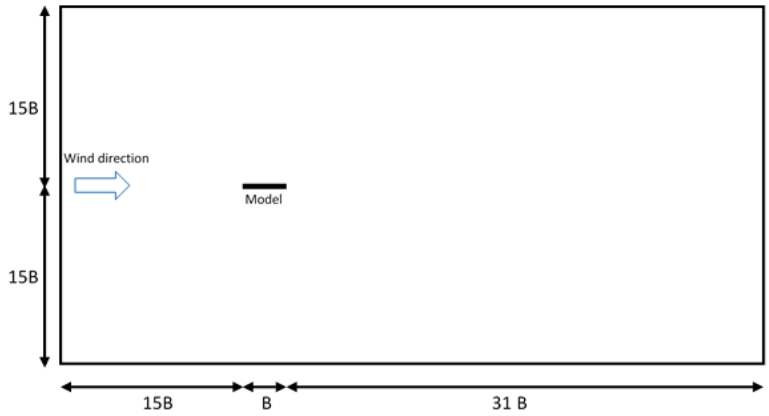

Figure 4. CFD domain design

After creating the domain, the next step is to generate the mesh, where the previously created domain is discretized into a mesh. The mesh generation is also performed using the Mesh Fluent ANSYS software module, which follows the Finite Volume Method concept. This study employs an unstructured mesh type, specifically tetrahedral mesh, due to its ease of implementation on complex geometries and shorter creation time than hexahedral mesh types. According to Kusuma et al. research [21,26], using tetrahedral mesh type is more optimal for complex and asymmetric geometries and more efficient in numerical simulation calculations. Like the model creation process, the bottom-up approach is used for meshing, which facilitates

placing the mesh near the desired model surfaces. In contrast to wind tunnel testing methods where the boundary layer is explicitly defined, according to Kasim et al., in CFD methods, the thickness of the boundary layer should be calculated based on input parameters since the domain is limited [27]. Improper estimation of the boundary layer thickness, as stated by Moukalled et al., can lead to suboptimal results and numerical simulation errors [28]. Jeremy et al. suggest that the simulated domain should be as large as possible to minimize the influence of the boundary layer when a model is isolated from the surrounding medium [29]. Salim et al. also mention that the virtual wind tunnel dimensions should be larger than the test model to avoid wind-structure interactions with the tunnel walls. Theoretically, the mesh's first boundary layer thickness (y^+) can be determined using Equation 1 [27].

$$y^+ \equiv \frac{u_* y}{v} \tag{1}$$

Where u_* is the model surface friction velocity, y^+ is the closest mesh distance to the model surface, and v is the kinematic velocity. However, due to numerical simulation hardware limitations restrictions, the y^+ used is around ±0.05 m, leading in a total mesh count of around ±5.5 million with an average orthogonal quality value of ±0.99 and a skewness value of ±0.83, which are within an acceptable range. In general, the principle of mesh generation is to limit cell size in the desired regions (e.g., areas with high pressure/velocity/gradients), such as the wing area of an aircraft. Figure 5 depicts the mesh near the object's surface and the boundary conditions applied.

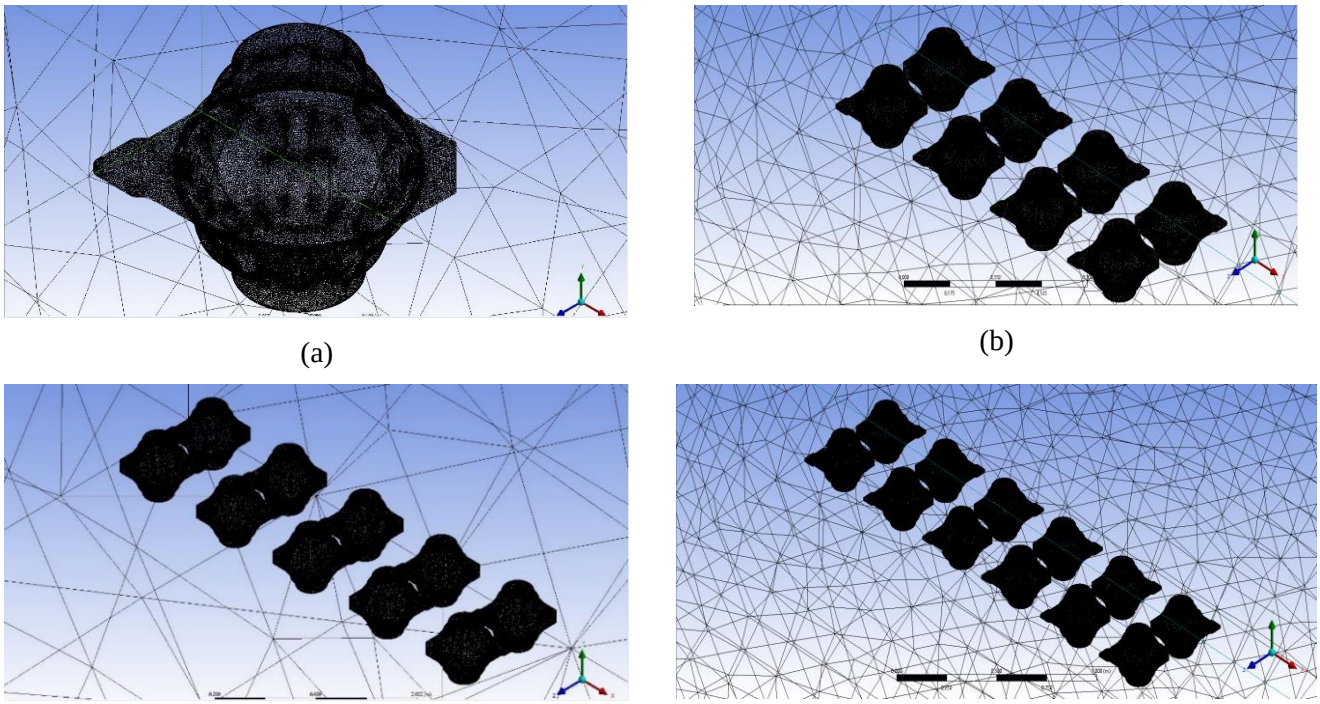

(a) (b) (c) (d)

Figure 5. (a) Mesh single, (b) Mesh 4 couples, (c) Mesh 5 couples, and (d) Mesh 6 couples.

2.3 Parameter inputs and convergence

After the mesh generation is completed, the next step is to determine the most appropriate parameters. Several variables need to be defined before performing calculations in the ANSYS Fluent software, such as fluid material properties, area, velocity/Reynolds number (*Re*), boundary conditions, and operating conditions, as shown in Table 1. In numerical simulations, determining the appropriate boundary conditions can significantly influence the numerical simulation output. The boundary conditions used in this study consist of inlet velocities (front, right, left, top, and bottom), wall boundaries (model surface), and outlet boundaries (rear) [23,25], as shown in Figure 6. The wall boundary conditions separate the fluid from the solid (model) region [22]. In this case, a no-slip assumption is applied to the wall boundary conditions,

assuming a smooth surface. The inlet velocity boundary conditions are used to determine the magnitude and direction of the velocity. Inlet velocity boundary conditions are commonly used for compressible flows. The inlet velocity boundary condition in this study involves both the magnitude and direction of the velocity, with the direction determined by the desired wind angle of attack [22]. The outlet boundary condition is used to model the outflow, where the pressure and velocity details are unknown before solving the flow problem [22].

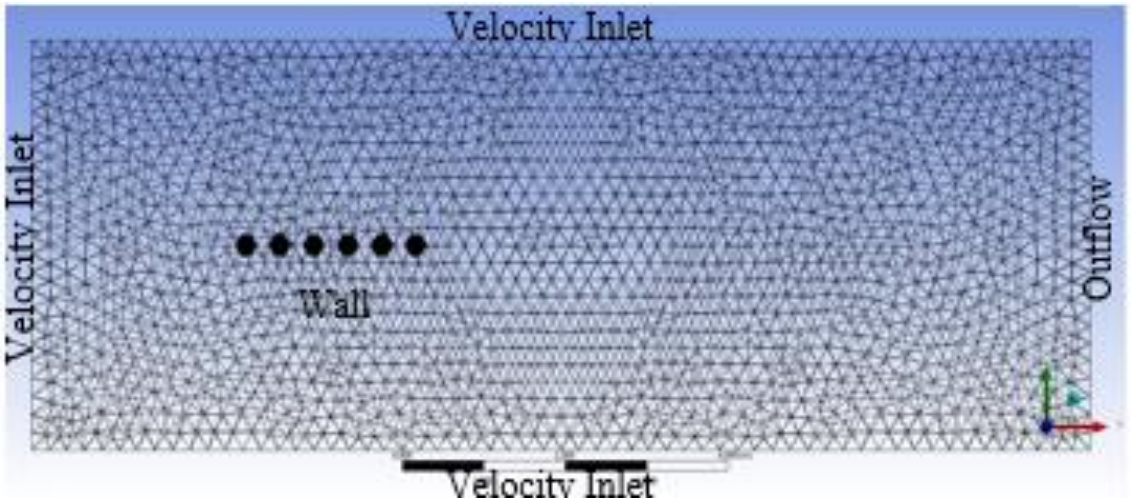

Figure 6. Boundary conditions

Once the boundary conditions are determined and the required parameters are inputted, the subsequent step involves setting up convergence criteria for the iterative process of the numerical simulation calculation. The number of iterations utilized directly impacts the time taken for the numerical simulation process. A more significant number of iterations prolongs the numerical simulation process, while fewer iterations expedite it. According to the references above, this numerical simulation process adopts a convergence criterion of 10^{-5}.

Table 1. Parameter inputs

Parameters	Single	4 Couples	5 Couples	6 Couples
Solver	K-omega SST			
Time type	Steady			
Density $[kg/m^3]$	1.225			
Viscosity [kg·s/m]	1.789×10^{-5}			
Area $[m^2]$	0.0708	0.1768		
Length [m]	0.285	1.4575	1.8960	2.2525
Reynolds number	3×10^5, 5×10^5, 7×10^5, 1×10^6, 2×10^6, 3×10^6			
The angle of attack [deg]	0			
Iteration	5.000 – 10.000			

Apart from setting the convergence criterion value, there are other ways to determine the convergence of the numerical simulation process by observing the coefficients that have become constant Figure 7. According to Kusuma et al. [21], the complexity of a model's shape influences convergence, with more complex shapes requiring more time to achieve convergence. Constant coefficient values throughout the iterations, according to Siti et al. [30], indicate that the numerical simulation process has converged.

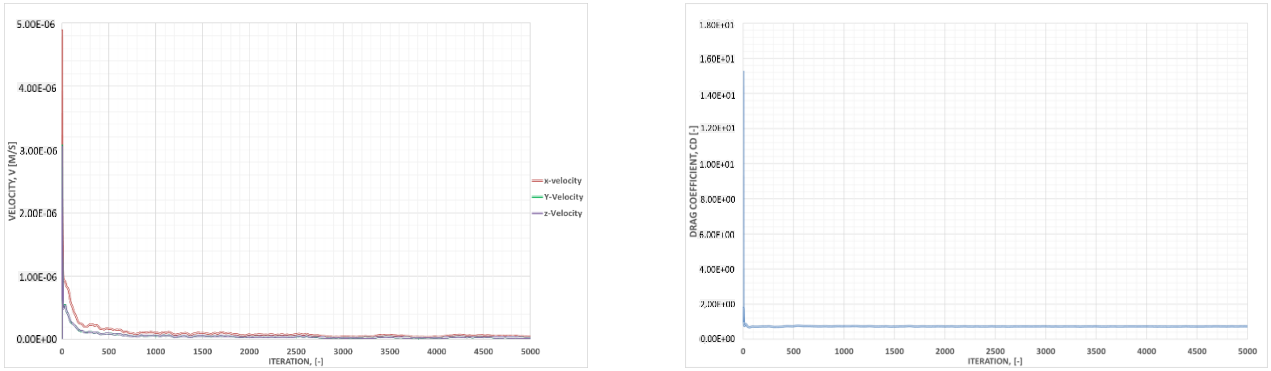

(a) (b)

Figure 7. Convergence criteria: (a) Residual, and (b) Drag coefficient

3 Results and Discussion

When the frictional drag dominates the drag force, an object can be considered streamlined. This consideration is due to the flow, which tends to adhere to the object as it passes through the fluid. On the other hand, when the drag force is dominated by pressure drag, the object is considered a bluff because the fluid leaves a wake behind the object after passing through. Therefore, only the frontal area is considered when bluff body surfaces are used as references. CFD simulations are run with two variations: six different Reynolds numbers and four different floating body configurations. The four floating body configurations consist of a single body, four couples, five couples, and six couples. The CFD results are displayed in the form of coefficient curves, as shown in Figure 8.

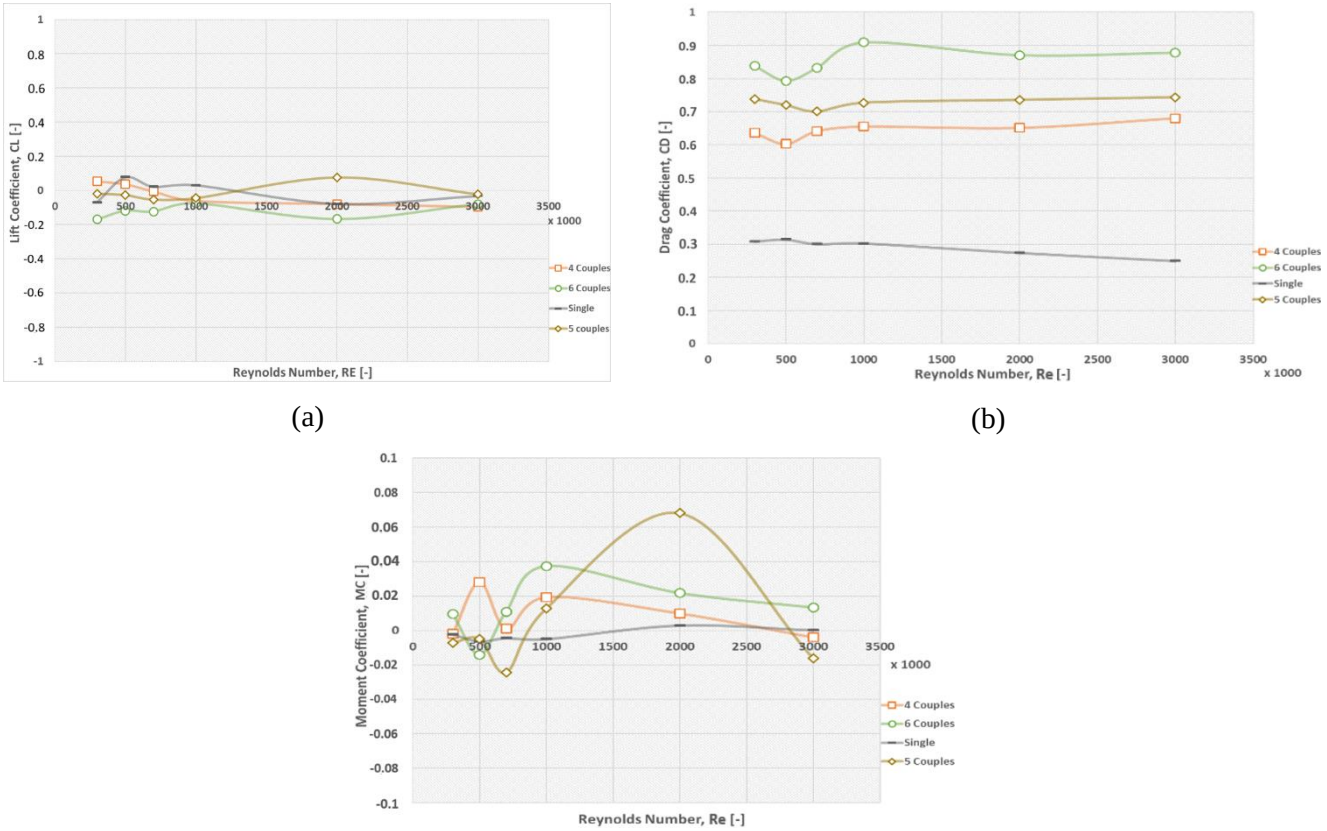

(a) (b)

(c)

Figure 8. Aerodynamics coefficient: (a) Lift, (b) Drag, and (c) Moment

Figure 8(a) shows that the 6 couples floater configuration (green line) has a better lift coefficient than the others. The negative values indicate this as the Reynolds number increases. The model is oriented

downwards as indicated by the negative sign. The other floater configurations, on the other hand, exhibit positive lift coefficient values at low Reynolds numbers that gradually become negative at higher Reynolds numbers. Figure 8(b) shows that each model produces similar graph patterns. Fluctuations in the coefficient values occur between Reynolds numbers 3×10^5 to 7×10^5, but after Reynolds number $> 7 \times 10^5$, the drag coefficient values do not change significantly. The single floater configuration (gray line) has the smallest drag coefficient for all Reynolds numbers, while the 6 couples floater configuration (green line) has the largest drag coefficient. The drag coefficient value also increases as the number of floater configurations increases. The drag coefficient difference between the single floater and couple floater configurations reach ≥ 50%. Regarding the moment coefficient in Figure 8(c), it can be observed that there are increases and decreases in almost all float configurations between Reynolds numbers 5×10^5 to 7×10^5, but after Reynolds number $> 1 \times 10^6$, the moment coefficient values do not change significantly except for the 5 couples float configuration with Reynolds number 2×10^6, which has the highest moment coefficient value. The CFD method has the advantage of allowing visualization of flow features such as velocity streamlines.

Figure 10 compares velocity streamlines for each floater configuration model at Reynolds numbers 5×10^5 and 2×10^6. Understanding the flow patterns around the floater configurations requires the visualization of velocity streamlines. Figure 10 shows how the number of float configurations affects the flow patterns and the coefficients values, particularly the drag coefficient. Figure 10 (a) shows that the single floater configuration exhibits a simpler flow pattern with a more uniform flow around the floater and a vortex occurring directly behind the floater model. On the other hand, as the number of floater configurations increases, the flow pattern becomes more complex, with more vortices forming between the floaters. The turbulent flow is caused by the interaction between the floater pairs. As turbulence or vortices increase, so do the drag coefficient values, improving the overall performance of the floater system. Overall, there are more vortices at Reynolds number 5×10^5, especially between the floater couples, than at Reynolds number 2×10^6.

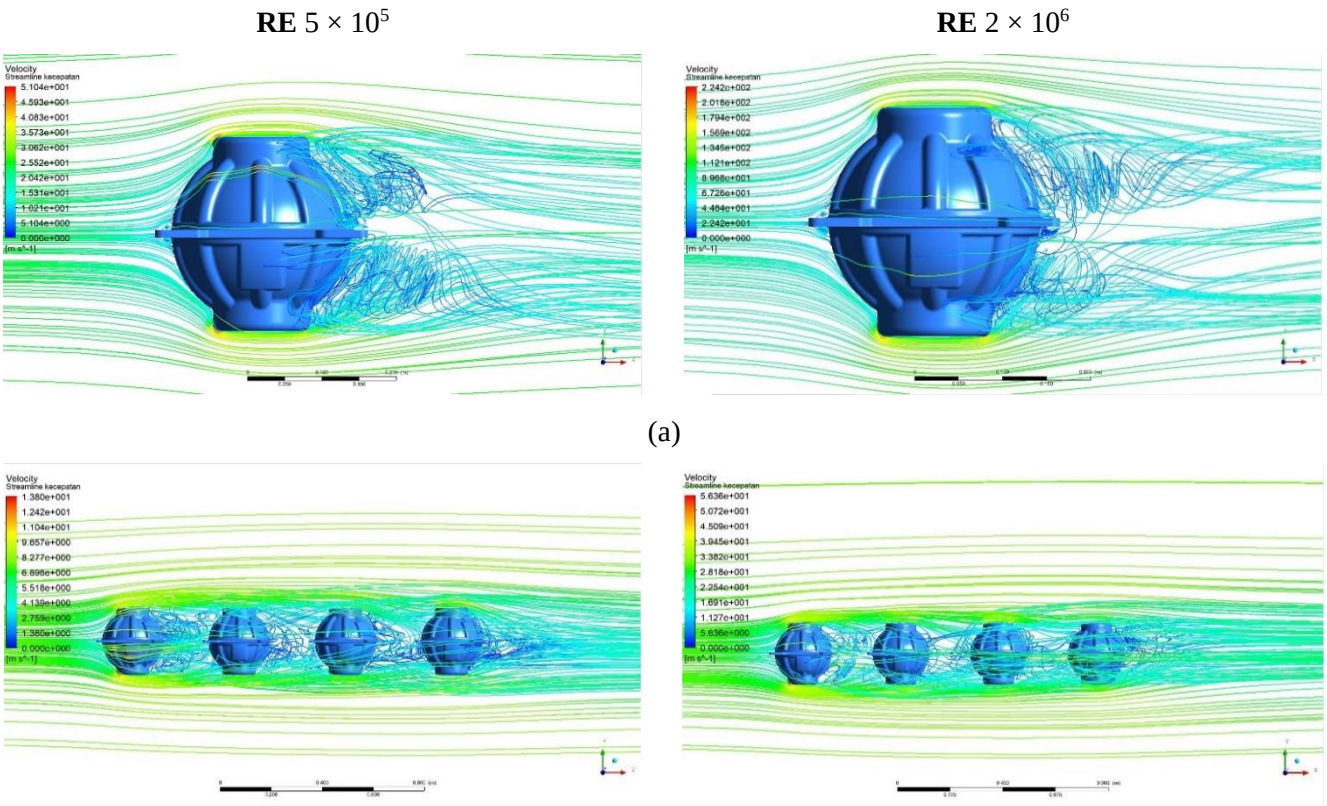

Figure 10. Velocity streamlines at RE 5×10^5 and 2×10^6 for floater OBU models: (a) Single, (b) 4 Couples, (c) 5 Couples, and (d) 6 Couples

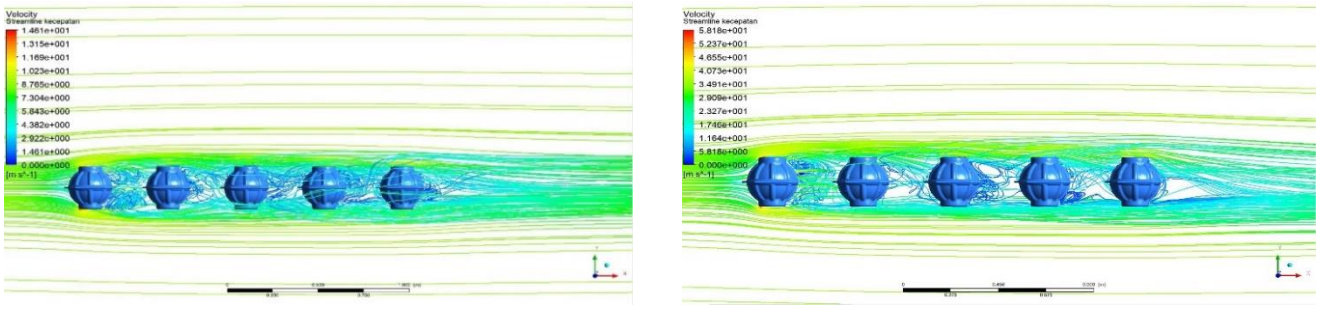

(c)

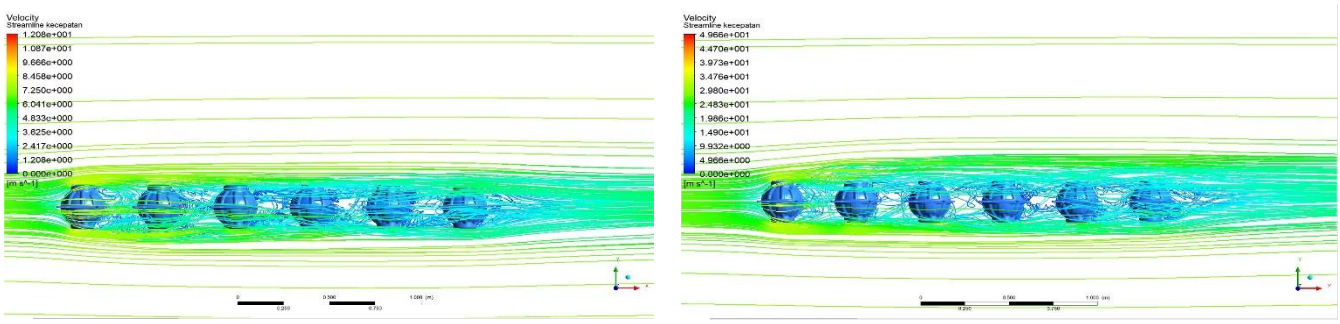

(d)

Figure 10. *Cont.*

4 Conclusions

The Computational Fluid Dynamics (CFD) analysis of the Ocean Bottom Unit (OBU) was performed in this study. The influence of the number of floater configurations on the Ocean Bottom Unit (OBU) flow pattern and drag performance is also being studied. The results show that the 6-couple floater configuration model exhibits better lift coefficient values than other floater configurations. Similarly, the six-couple float configuration model also has the highest drag coefficient value, enabling it to withstand forces caused by wind and waves for all Reynolds numbers. In terms of moment coefficient, nearly all floater configurations experience an increase or decrease in the range of $5 \times 10^5 \leq Re \leq 7 \times 10^5$, but after $Re \geq 1 \times 10^6$, the moment coefficient values do not change significantly, except for the 5 couples floater configuration model, which has the highest moment coefficient value. Increasing the number of floater configurations can result in higher drag coefficients and lower lift coefficients. The percentage of difference in drag coefficient between the single floater and couple floater configurations reach ≥ 50%. Meanwhile, the average percentage difference in the drag coefficient between paired float configurations ranges from 11% to 24%. The visualization of velocity streamlines reveals that the number of floater configurations influences the flow patterns and coefficient values. The single floater model exhibits a simple flow pattern, while models with multiple floater configurations display more complex flow patterns due to more vortices. This phenomenon results from the interaction between the couple floaters, creating turbulence behind the floater configurations. The more configurations, the more vortices occur, thereby influencing the coefficients in the float.

In the future, it is expected that several studies will be conducted using numerical simulations and experiments on various configurations of the number of Ocean Bottom Unit (OBU) floaters and the spacing between them. It is hoped that by determining the optimal number and spacing of OBU floaters, the best drag coefficients for practical application can be obtained. Furthermore, it is expected that further research will contribute to enrich the database for a crucial component of the tsunami early warning system.

5 Acknowledgement

The authors would like to thank the lead researcher for the floater OBU, and the computation in this work has been done using the facilities of Workstation and Software ANSYS at the National Laboratory of Aerodynamics, Aeroelastic, and Aeroacoustics (LA3), Directorate of Laboratory Management, Research, Facilities, and Science and Technology Park, National Research and Innovation Agency (BRIN).

References

1. S. Hadi, S. Widayani, and S. A. Mulyo, *Disaster Management Master Plan 2015 – 2045*. Jakarta: Badan Nasional Penanggulangan Bencana, 2018. (*in Indonesian*).
2. L. Hamzah, N. T. Puspito, and F. Imamura, "Tsunami Catalog and Zones in Indonesia," *J. Nat. Disaster Sci.*, vol. 22, no. 1, pp. 25-43, 2000.
3. B. A. Hakim, S. Suharyanto, and W. K. Hidajat, "Pengaruh kenaikan air laut pada efektifitas bangunan untuk perlindungan pantai kota Semarang," *Buletin Oseanografi Marina*, vol. 2, no. 3, pp. 81-93, 2013. (*in Indonesian*).
4. D. Ghosh, A. K. Mittal, and S. Bhattacharyya, "Multiphase Modeling of Tsunami Impact on Building with Openings," *J. Comput. Multiph. Flows*, vol. 8, no. 2, pp. 85-94, 2016.
5. P. Bird, "An Updated Digital Model of Plate Boundaries," *Geochemistry Geophys Geosystems*, vol. 4, no. 3, article no. 1027, 2003.
6. C. DeMets, R. G. Gordon, and D. F. Argus, "Geologically Current Plate Motions," *J. Int. Geophys.*, vol. 181, no. 1, pp. 1-80, 2010.
7. Pusat Studi Gempa Nasional, *Peta Sumber dan Bahaya Gempa Bumi Indonesia Tahun 2017*, Jakarta: Kementerian Pekerjaan Umum dan Perumahan Rakyat, 2017. (*in Indonesian*).
8. T. Gunawan, A. G. Ginanjar, N. Pimpilemba, I. Gunawan, M. Riyadi, S. Nugroho, and P., *Indonesia Tsunami Early Warning System: Concept and Implementation*, Jakarta: Agency for Meteorology Climatology and Geophysics, 2016.
9. R. Triyono, T. Prasetya, S. D. Anugrah, A. Sudrajat, U. Setiyoo, I. Gunawan, P. T. Yatimantoro, H. S. Anggraini, R. H. Rahayu, D. S. Yogaswara, P. Hawati, M. Apriani, A. M. Julius, M. Harvan, G. Simangunsong, and T. Kriswinarso, *Katalog Tsunami Indonesia Per-Wilayah Tahun 416-2018*, Jakarta: Badan Meteorologi Klimatologi dan Geofisika, 2018. (*in Indonesian*).
10. Supartoyo, Surono, and E. T. Putranto, *Katalog Gempabumi Merusak di Indonesia Tahun 1612-2014*, Bandung: Pusat Vulkanologi dan Mitigasi Bencana Geologi, 2014. (*in Indonesian*).
11. W. H. Nugroho, N. J. H. Purnomo, O. Ivano, and S. Handoyo, "Rekayasa Desain dan Analisis Struktur perangkat dasar laut Ocean Bottom Unit (OBU) untuk INA – TEWS," *Jurnal Rekayasa Energi Manufaktur*, vol. 1, no. 2, pp. 49-56, 2016.
12. D. Monardo, *National Disaster Management Plan 2020-2024*. Jakarta: Badan Nasional Penanggulangan Bencana, 2020.
13. BNPB, *National Disaster Management Agency Strategic Plan 2015-2019*. Jakarta: Badan Nasional Penanggulangan Bencana, 2015.
14. A. Arif, I. Rafliana, A. M. Kodijat, and S. Dalimunthe, *Limitations and Challenges of Early Warning Systems Case Study: Palu-Donggala Tsunami*, Jakarta: United Nations Office for Disaster Risk Reduction, 2019.
15. W. H. Nugroho, B. A. Hakim, and A., *Rancang Bangun INA Buoy Gen. 3 untuk Sistem Peringatan Dini Tsunami*, Surabaya: ITS Press, 2021.
16. Arifin, W. H. Nugroho, B. A. Hakim, and Suwahyu, "Numerical Study of Environment Loads and Mooring Line Scope Effects to The Buoy Offset," *IOP Conf. Ser. Earth. Envi. Sci.*, vol. 972, no. 1, article no. 012009 2021.
17. M. Sadraey, *Chapter 3: Drag Force and Drag Coefficient - Aircraft Performance Analysis*, Riga: Omniscriptum, 2018.
18. J. Almedeij, "Drag Coefficient of Flow Around a Sphere: Matching Asymptotically The Wide Trend," *Powd. Tech.*, vol. 186, no. 3, pp. 218-223, 2008.
19. M. Irfan, Y. Haryadi, D. Haryanto, and A. Rusdiansyah, "Technical Review of the Placement of the Mooring Buoy and INA-TEWS System on the Seabed," *Jurnal Riset dan Rekayasa Kelautan*, vol. 2, no. 1, pp. 1–16, 2021. (*in Indonesian*).
20. Arifin, H. N. Wibowo, H. Buddin, and W. Bambang, "Numerical Prediction of Foils Configuration in A Design of Buoy Glider System for Supporting Tsunami Early Warning," *IOP Conf. Ser. Mat. Sci. Eng.*, vol.

1052, no. 1, article no. 012017, 2020.
21. Y. F. Kusuma, H. Defianti, F. Hasim, and F. A. Yohanes, "Effect of Additional Fin and Thickness of Basic Plate of The Ocean Bottom Unit (OBU) Model Using Computational Fluid Dynamics," *AIP Conf. Proc.*, vol. 2646, article no. 050080, 2023.
22. F. Tuakia, *Dasar-dasar cfd menggunakan fluent*, Bandung: Informatika, 2008.
23. N. Nisa, "Studi Numerik Karakteristik Aliran Fluida pada Airfoil NASA LS-0417 yang Dimodifikasi dengan Vortex Generator," *POMITS*, vol. 1, no. 2, pp. 1-6, 2012. (*in Indonesian*).
24. L. Bruno and S. Khris, "The Validity of 2D Numerical Simulations of Vortical Structures Around a Bridge Deck," *J. Math. Comput. Model.*, vol. 37, no. 7-8, pp. 795-828, 2003.
25. S. C. Chapra and R. P. Canale, *Numerical Method For Engineers*. New York: Mc Graw-Hill, 2010.
26. ANSYS, *ANSYS Fluent Theory Guide Release 15.0*, Pennsylvania: ANSYS Inc., 2013.
27. S. M. Salim and S. Cheah, "Wall y+ Strategy for Dealing with Wall-bounded Turbulent Flows," in *the International MultiConference of Engineers and Computer Scientists*, Hong Kong, Hong Kong, 2009.
28. F. Moukalled, L. Mangani, and N. Darwish, *The Finite Volume Method in Computational Fluid Dynamics*, Berlin: Springer International Publishing, 2016.
29. J. D. Bricker, K. Kawashima, and A. Nakayama, "CFD Analysis of Bridge Deck Failure Due to Tsunami," in *the International Symposium on Engineering*, Tokyo, Japan, 2012.
30. S. N. Rahmah, *Analisis Aerodinamika Aileron Pesawat N2XX dengan Metode Computational Fluid Dynamics*, Jember: Universitas Jember, 2020.